ORIGINAL RESEARCH

Process analyses of friction drilling using the Smoothed Particle Galerkin method

Eugen Stockburger[1] · Wanmu Zhang[1] · Hendrik Wester[1] · Daniel Rosenbusch[1] · Bernd-Arno Behrens[1]

Abstract

As a cost-effective hole production technique, friction drilling is widely used in industrial and automotive manufacturing. Compared with the traditional bolted connection, it enables the fastening of thin metal sheets and thin-walled tubular profiles. Friction drilling results in higher thread length and joint strength, thus better fulfilling the demand for lightweight structures. However, in the numerical simulation of friction drilling, the traditional finite element method encounters difficulties caused by the extreme deformation and complex failure of the material. A large number of elements are usually deleted due to the failure criterion, which significantly reduces the solution accuracy. The development of meshless methods over the past 20 years has alleviated this problem. Especially the Smoothed Particle Galerkin (SPG) method proposed in recent years and incorporating a bond-based failure mechanism has been shown to be advantageous in material separation simulations. It does not require element removal and can continuously evolve each particle's information such as strain and stress after the material failure. Therefore, the SPG method was used in this research for the simulation of frictional drilling of HX220 sheet metal. First the particle distance and the friction coefficient were varied to investigate the applicability of the SPG method to the friction drilling process. Predicted and experimental results were compared and found to be in high agreement. Furthermore, the influence of input parameters, such as sheet thickness, feed rate and rotational speed, on axial force as well as torque of the tool and the surface temperature of the workpiece during friction drilling was investigated numerically.

Keywords SPG method · Friction drilling · Experimental validation · Sensitivity study · HX220 sheet steel

Introduction

Friction drilling

In the friction drilling process, also named thermal drilling, flow drilling, thermo-mechanical drilling, friction stir drilling and form drilling [1], heat is generated by friction between the drill made of a hard material like tungsten carbide and the metallic workpiece. The induced heat softens the workpiece material and the drill passes through the workpiece under the combination of axial force and high speed rotation, causing the material to be squeezed and to flow up as well as down forming the upper and lower bushing. Figure 1 depicts the friction drilling process, which is not a separating process, but rather a process of joining by forming. The total height of the formed bushing is usually two to three times the thickness of the original workpiece, with the lower bushing height generally accounting for two-thirds of the total height [1]. Additionally, a thread can be formed in the produced bushing to create a detachable connection of thin-walled workpieces. By using the friction-drilled bushing, a longer thread length can be applied, which makes the connection more reliable in comparison to traditional joining methods by bolt and nuts.

Due to the increasing demand for lightweight structures, friction drilling has been more and more widely used in thin-walled sheet metals and tubular workpieces in recent years. In order to predict the process parameters of friction drilling, methods such as artificial neural network (ANN) [2], genetic algorithm (GA) [3] and fuzzy logic algorithms [4] have been proposed to predict the length and roughness of bushings with good results. Moreover, image-based modelling is a necessary tool for understanding material flow, temperatures, stresses and strains during friction drilling,

✉ Eugen Stockburger
  stockburger@ifum.uni-hannover.de

1 Institut für Umformtechnik und Umformmaschinen (IFUM),
   Leibniz Universität Hannover, An der Universität 2,
   30823 Garbsen, Germany
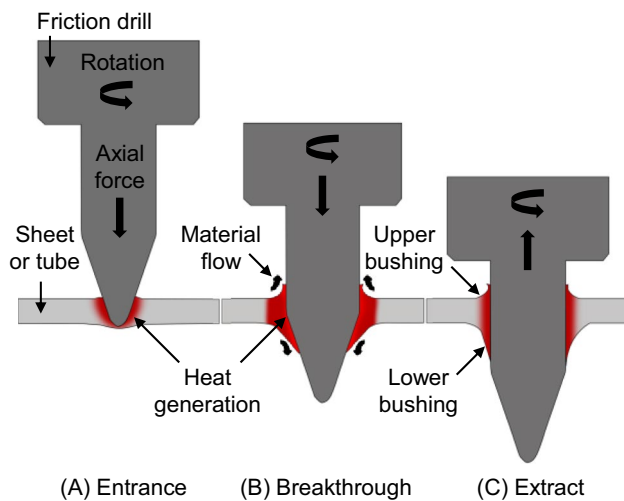
Fig. 1 Illustration of the friction drilling process

which are difficult to measure by experiment [5]. The modelling of friction drilling can be used to reduce the number of experiments, because the optimal process parameters can be obtained based on accurate process predictions [6]. Until now, the majority of numerical method studies of friction drilling were based on the finite element method (FEM) [7]. However, the traditional mesh-based methods suffer from mesh distortion when dealing with problems such as friction drilling with large deformations [8]. This often leads to numerical difficulties, such as non-convergence of implicit simulations or instability of explicit simulations. However, mesh-based methods inevitably delete elements when dealing with extreme deformations and material failures, which can render it difficult to maintain a high-quality mesh or make the adaptive mesh unstable [9]. In addition, the element erosion technique leads to a loss of mass as well as energy and will affect the stress responses in friction drilling. This can also seriously affect the accuracy of the computational results and even lead to erroneous failure predictions. Therefore, the material flow and the formation of high-quality upper and lower bushings are difficult to achieve when using FEM to simulate friction drilling.

Smoothed Particle Galerkin method

To overcome the inherent shortcomings of mesh-based methods, more than 20 meshfree methods and correction schemes have been proposed in the past few decades. The effectiveness of the meshfree methods has been demonstrated for large deformations [10], impact problems [11] and evolving cracks [12]. In contrast to the mesh-based finite element method, the meshfree methods use a set of particles to discretize the solving region and to construct an approximation function, which does not require the

division of the mesh or remeshing. However, meshfree methods also have their own drawbacks. Compared with FEM, meshfree methods cause higher computational costs and the application of essential boundary conditions is more difficult.

The first meshfree method is generally considered to be the Smoothed Particle Hydrodynamics (SPH) method, developed by Gingold and Monaghan [13] and Lucy [14] in 1977. It was primarily used in the field of astrophysics, later in fluid mechanics [15] and solid mechanics [16]. However, the SPH method suffers from three instability problems [17] that seriously affect the numerical convergence, namely tensile instability, rank deficiency and material instability. Some schemes and new methods have been proposed to improve these problems, among which Belytschko et al. [18] and Liu et al. [19] developed the Element Free Galerkin (EFG) method and the reproducing kernel particle method (RKPM). However, the EFG method needs a background integral mesh. When the material is damaged, the background integral mesh needs to be re-established, so it is not recommended for failure analysis. The stabilized conforming nodal integration (SCNI) method developed by Chen et al. [20] in 2001 employs a strain smoothing stabilization for nodal integration and does not involve numerical control parameters, significantly improving accuracy and convergence rate for the meshfree method using direct nodal integration (DNI). However, the SCNI method still cannot be separated from the background mesh. A new meshfree method, the Smoothed Particle Galerkin (SPG) method, proposed by Wu et al. [21] in 2015 provides a better solution to the separation problem.

SPG is a meshfree Galerkin method using the DNI technique. However, the use of DNI is prone to the hourglass problem (zero energy). So, in order to obtain a converged numerical solution, an additional non-residual penalty–type enhancement stabilization term based on the so-called displacement smoothing theory is added. The semi-discrete equations of motion for solving explicit dynamics problems can generally be written as

$$M\ddot{u} = f^{ext} - f^{int} \tag{1}$$

where M is the mass matrix, $\ddot{u}$ is the acceleration, f^{ext} is the external force vector and f^{int} is the internal force vector. The internal force term needs to be calculated for each particle at each time step, which is very time-consuming. Therefore, the DNI technique with displacement smoothing scheme is adopted to improve efficiency. Thus, the equation of motion to be solved can be written as

$$M\ddot{u} = f^{ext} - f^{int} - \widehat{f}^{stab} \tag{2}$$

where $\widehat{f}^{stab}$ is the stabilization term derived from the smooth displacement theory. It can be calculated by DNI

$$\widehat{\boldsymbol{f}}^{stab} = \sum_{N=1}^{NP} \widehat{\boldsymbol{B}}_I^T(X_N)\widehat{\boldsymbol{\sigma}}(X_N)J^0 V_N^0 \tag{3}$$

where J^0 is the determinant of the Jacobian matrix, V_N^0 is the volume of particle N, $\widehat{\boldsymbol{B}}_I^T$ is the stabilization gradient matrix associated with the displacement smoothing function and $\widehat{\boldsymbol{\sigma}}$ is the stabilization stress. The complete derivation process and the calculation of gradient matrix as well as stabilization stress are documented by Wu et al. in [21] and [22].

To simulate the material separation as well as failure more physically and to avoid potential spurious damage growth issues with meshfree approximations used in material failure analysis, a bond-based failure mechanism is also proposed under the framework of SPG [23]. This means that each SPG particle has an influence domain of a certain size and the connection between each particle within the domain is defined as a bond. When a part reaches a user-defined failure criterion during plastic deformation, such as a limit for the effective plastic strain, the bond breaks and the material fails. This has no effect on other particles and bonds in the domain, except that there is no longer any interaction between the two particles originally connected. Therefore, the subsequent stress and strain can still be given by the material constitutive laws. This avoids loss of material, momentum and energy caused by element deletion and stress nulling in contrast to FEM.

Forming simulations using particle methods

Due to the advantages of particle methods for the simulation of large deformation in materials, more and more forming simulations have adopted particle methods in the past 20 years. Most of these studies employed relatively mature meshless methods, such as SPH, RKPM and EFG. Among them, Prakash and Cleary used the SPH method to simulate the extrusion process of cylindrical aluminium alloy billet with a diameter of 40 mm in 2006 [24]. A total of 7760 SPH particles were used in the 3D model with a spacing of 1.6 mm. The simulation results demonstrated the high plastic strain of the extrusion process well and the effects of die geometry such as the extrusion ratio and die angle on the strain as well as maximum extrusion force are predicted. Prakash et al. also performed 2D simulations of different types of forging processes for aluminium alloy A6061 using the SPH method. The material deformation and flow during forging were studied, also forging defects such as flashing as well as incomplete die filling are effectively simulated and predicted. Furthermore Reddy et al. [25] used the SPH method to simulate multi-die forging of industrial components and verified the accuracy of the SPH by comparing the results with the FEM in a uniaxial compression simulation. Bonet and Kulasegaram [26] adopted the corrected smooth

particle hydrodynamics (CSPH) with an integral correction and a least-squares stabilization method to further improve the consistency and stability. The effectiveness of the CSPH method in metal forming such as axisymmetric forging and plane strain upsetting was demonstrated.

In 1998, Chen et al. [27] first applied the RKPM to large deformation and metal forming analysis. A Lagrangian RKPM with material loading path-dependent behaviour and frictional contact conditions based on a penalty method was proposed to ensure stability in large deformation analysis. This method showed to be in high agreement with the membrane analytical solution in the prediction of metal punch stretching. Its effectiveness has also been demonstrated in ring compression and upsetting analysis. Shangwu et al. [28] developed a flow formulation of rigid-plastic materials based on the RKPM approach for slightly compressible material models. The simulation results for flat rolling, compression of rods and heading of cylindrical billets were in good agreement with FEM and experimental results. Liu et al. [29] proposed a low order integration scheme to improve the computational efficiency of RKPM, which is suitable for bulk metal forming simulations such as forging and backward extrusion. Furthermore, RKPM is also used to simulate splitting rolling [30], wheel forging analysis [31] and deep drawing [32].

In 2001 Li and Belytschko [33] first demonstrated the effectiveness of the EFG method in metal forming simulations such as upsetting, rolling and extrusion processes. Xiong et al. further showed how effective the combination of EFG and slightly compressible rigid–plastic material models [34] and the combination of EFG and the boundary element method (BEM) [35] in the prediction of plane strain rolling results are. Guan et al. [36] proposed an EFG method based on the hypothesis of a visco-plastic material, which is suitable for the metal forming analysis of arbitrarily shaped dies. Yonghui et al. [37], Lu et al. [38] and Liu et al. [39] verified the agreement between the EFG method and FEM for the numerical analysis of bulk metal forming. Yuan et al. [40] and Wang et al. [41] applied the EFG method to simulate a sheet metal flexible-die forming process and the results were in agreement with FEM as well as experimental results.

Furthermore, there are some other types of meshfree methods used for forming simulations. Alfaro et al. [42] verified the applicability of the natural element method (NEM) based on α-shapes node cloud scheme, which makes the treatment of essential boundary conditions more reliable, for 3D thermal simulations of extrusion forming of aluminium alloys. Filice et al. [43] and Lu et al. [44] also demonstrated the effectiveness of NEM for numerical computations of metal forming. Yoon et al. [45] proposed an accelerated meshfree method based on a stabilized conforming nodal integration method and the introduction of strain smoothing stabilization, which significantly improves the

computational accuracy of metal forming. Kwon et al. [46] proposed a new meshfree method based on an elastic–plastic first-order least-squares formulation, which represents the residuals in the form of a first-order differential system using displacement and stress components as nodal unknowns. Its effectiveness was verified in numerical simulations of metal forming such as ring compression and axisymmetric forging. Hah and Youn [47] proposed an Euler meshfree method using non-uniform rational B-spline (NURBS) curves as a boundary representation. This method eliminated the need to solve convection transport equations in the traditional Euler framework and the obtained results of the rigid-plastic analysis in the bulk metal forming process were consistent with the experimental and other numerical methods.

In practical applications, the SPG method has proven its effectiveness and accuracy in large deformation simulations such as high-speed metal grinding of aluminium alloys [48], self-piercing rivet (SPR) connections of aluminium alloys [49], penetration and perforation analysis of metal targets [50] and friction drilling [51]. On this basis, Wu et al. further developed a momentum-consistent smoothed particle Galerkin (MC-SPG) method for simulating friction drilling [52] and the flow drill screw-driving process [53]. The main improvement of this method is the introduction of a new velocity smoothing algorithm that consistently satisfies the conservation of momentum to stabilise the formulation. Therefore, the method does not require any additional stabilisation term making it more efficient. A comparison of simulation results and experimental data shows that this method predicts the response of force and torque very accurately.

However, almost all simulations of friction drilling using numerical methods to date have not considered the formation of the bushing on the specimen. FEM models were used to study process parameters like axial force and torque, while the SPG method was used to study the sensitivities of the computational parameters in friction drilling processes. Therefore, in this paper, the SPG method is investigated regarding its applicability to friction drilling of HX220. The particle distance as well as the friction coefficient were varied and validated with experiments regarding axial force, temperature evolution in the specimen as well as material flow of the bushing. Based on the SPG model the input parameters sheet thickness, feed rate and rotation speed are numerically investigated.

Materials and methods

SPG modelling

The SPG method was used to model a friction drilling process with particle methods. For this purpose, a 3D simulation model was created in the pre-processor LS-PrePost

and calculated with the LS-DYNA solver. To create the numerical models, the effective parts of the tools and the specimen were abstracted, processed and discretized. The set-up corresponds to that of the experimental investigations, consisting of the friction drill and the specimen, which are shown in Fig. 2. The specimen corresponds to a cylinder with a diameter of 10 mm and a thickness of 1.2 mm. The distance between the particles was set to 0.4 mm and at the deformation area in the centre of the specimen with a diameter of 5 mm a denser particle distance of 0.2 mm was used resulting in a total of 7350 particles. An M4 friction drill with a diameter of 3.7 mm was modelled. The contour of the friction drill with the forming lugs was simplified and assumed to be rotationally symmetric. For discretization of the friction drill, shell elements with an element edge length of 0.2 mm with a refinement of 0.05 mm at the top of the drill resulting in 3331 elements were used.
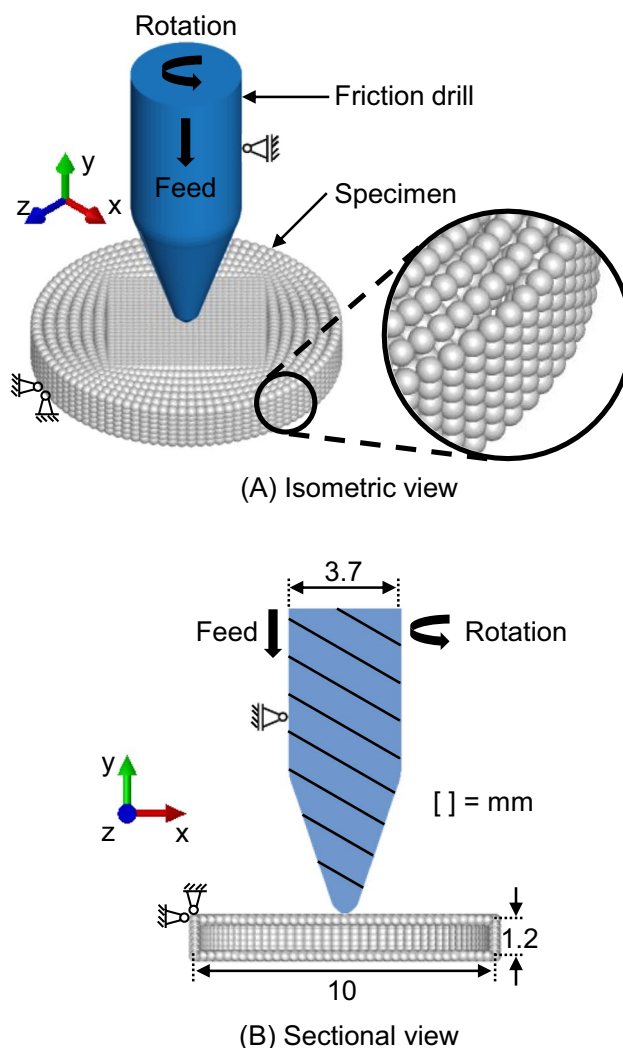
Fig. 2 Geometry and boundary conditions of the SPG model for friction drilling with rotational speed and feed rate

The boundary conditions were chosen based on friction drilling tests. Due to the very complex physical phenomena of the friction drilling process, several assumptions were made in the numerical model. For example, friction during friction drilling is a complex and changing condition. The friction parameters are difficult to determine experimentally and therefore the friction between the specimen and the friction drill was simplified using Coulomb's law of friction with a friction coefficient of 0.3. The contact between the specimen and the friction drill was modelled with automatic nodes to surface contact using the penalty method. The outer edge of the specimen was fixed in all rotational and translational directions, whereas the friction drill was only movable in the y-direction and rotatable around the y-axis. A rotational speed of 5800 rpm and a feed rate of 50 mm/min were used for the friction drill.

The specimen material HX220 was modelled elastic–plastic using the Johnson–Cook hardening model [54] based on literature data from Behrens et al. [55]. In the J-C hardening model, flow stress k_f is analytically determined by plastic strain ε_{pl}, plastic strain rate $\dot{\varepsilon}_{pl}$, and temperature T

$$k_f = \left(A + B \times \varepsilon_{pl}^n\right)\left(1 + C \times ln\frac{\dot{\varepsilon}_{pl}}{\dot{\varepsilon}_0}\right)\left(1 - \left(\frac{T - T_{room}}{T_{melt} - T_{room}}\right)^m\right) \quad (4)$$

where $\dot{\varepsilon}_0$ is the reference plastic strain rate, T_{room} is the room temperature, T_{melt} is the melting temperature of the material, and A, B, C, m, n are material parameters. The parameters of the Johnson–Cook hardening model used are summarized in Table 1. Due to the material parameter C being equal to zero, the material is modelled strain rate independent. The Young's modulus of the specimen was set to 210 GPa, the Poisson's ratio to 0.3 and the density to 7850 kg/m³. To predict the failure of the specimen, the bond failure mechanism based on the effective plastic strain at failure 0.4 was used, which was obtained by an FE simulation of the tension test in [55]. Additionally, the thermal properties of the specimen material HX220 used are heat capacity 500 J/kgK, thermal conductivity 50 W/mK and thermal expansion coefficient 15×10^{-6} 1/K. Furthermore, as a thermal boundary condition to model the heat flux in the experiment convection was applied to the specimen using a heat transfer coefficient to air of 5 W/m²K assuming free flow. The heat conduction of the material is assumed to be isotropic and all heat during

friction drilling is generated by plastic deformation as well as friction between the drill and the specimen, ignoring thermal radiation at the contact surfaces due to its low influence. The friction drill was modelled as a heat conductive rigid body made of tungsten carbide with a heat capacity of 280 J/kgK and a thermal conductivity of 85 W/mK.

Since the calculation of the models requires a small time step to ensure the stability of the calculation, which will lead to a very long calculation time, a mass scaling factor of 100 and a time scaling factor of 100 were adopted to improve the computational efficiency. For the calculation, a cubic spline was used as the kernel function with an Eulerian kernel approximation that is suitable for large deformation and failure analysis of ductile materials. The normalized support size of particles in three directions of space DX, DY and DZ was set to 1.9 to ensure the stability of the calculation. The parameter SMSTEP, which gives the frequency of the numerical displacement smoothing by the number of time steps, was set to 50 to reduce the calculation. An iterative solver and the explicit calculation method with hourglass control were used for the coupled thermo-mechanical analysis. The LS-DYNA solver R12.0 with double precision was applied and the calculation took about 22 h utilising the Intel(R) Xeon(R) CPU E5-2680 v4 with 2.4 GHz and 16 cores.

Since a slight change in the process conditions of friction drilling can greatly affect the complex process behaviour [56], the SPG method was studied in this paper and qualitative comparisons were made. By varying different parameters, the applicability of the SPG method to friction drilling and the effect of the friction drilling input parameters to the quality of the results could be investigated. In Table 2, the parameter variations are depicted.

First, parameters for the applicability of the SPG method were studied. The particle distance was varied (study 1). Next, the SPG method was analysed for different friction coefficients (study 2). Both applicability parameters were studied for their effect on friction drilling regarding the axial force as well the torque of the tool and the surface temperature as well as material flow of the specimen. Further, a comparison to experimental results for validation purposes was performed (study 3). The input parameters studied in this paper are the specimen thickness (study 4), the tool feed rate (study 5) and the rotational speed of the spindle (study 6).

Table 1 Parameters of the used Johnson–Cook hardening model [55]

Parameter	A	B	C	m	n	$\dot{\varepsilon}_0$	T_{room}	T_{melt}
Unit	MPa	MPa	-	-	-	s⁻¹	°C	°C
Value	212.2	409.2	0	0.7521	0.3524	0.01	20	1500

Table 2 Studied parameter variations on the SPG friction drilling simulation

Study	Applicability			Input parameters		
Parameter	Particle Distance d	Friction Coefficient μ		Sheet Thickness t	Feed Rate f	Rotational Speed v
Unit	mm	-		mm	mm/min	rpm
1	0.1; 0.2; 0.3; 0.4; 0.5	0.3		1.2	50	5800
2	0.2	0.1; 0.2; 0.3; 0.4; 0.5				
3		0.3				
4				1; 1.2; 1.5		
5				1.2	30; 50; 70	
6					50	4800; 5800; 6800

The effects of the input parameters were compared regarding axial force, torque, temperature and the resulting bushing. All other settings in the simulations of the parameter studies were kept constant, only the corresponding parameter was changed.

Validation experiment

The model and the main input parameters used in the simulations must be consistent with the experimental conditions for comparisons to be meaningful. Therefore, experimental tests were utilized to validate the particle simulations. The test setup was installed in a 5-axis DMU 100 Monoblock milling machine from DMG MORI, consisting of a friction drill, a specimen, a clamping and force measuring plates. An M4 friction drill and a separating agent were used for the tests. The tested rotational speed and feed rate were 5800 rpm and 50 mm/min. For testing, specimens made of the HX220 steel with a thickness of 1.2 mm were used. Since direct temperature measurement on the bushing during the test is problematic due to the setup of the experiment and the rapid temperature changes, thermocouples were welded onto the sheet located at about 4 mm from the centre to measure the surface temperature on the specimen. The axial drilling force during friction drilling was measured with a force measuring plate. Further, the contour of the bushing was optically captured by microscope images. Therefore, experiments were performed and stopped after different forming depths. Using a VR-3200 3D profilometer from Keyence, optical images as well as 3D profiles of the upper and lower bushing were taken after complete forming. The input parameters and the experimental process of friction drilling are described in detail by Behrens et al. in [55]. Important results of friction drilling, namely axial force, temperature and bushing form will be compared with the simulation in order to validate the results.

Results and discussion

Investigation on the applicability of the SPG method to friction drilling

Variation of the particle distance

Figure 3 shows the plastic strain distribution at the extract as a contour plot for a variation of the particle distance between 0.1 and 0.5 mm with a step size of 0.1 mm, while keeping the other parameters constant. The total bushing length decreases with increasing particle distance from 4.18 to 3.01 mm. As can be seen, both the upper and lower bushing turn out smaller for higher particle distances. With smaller particle distance, the thickness of the bushing can be mapped
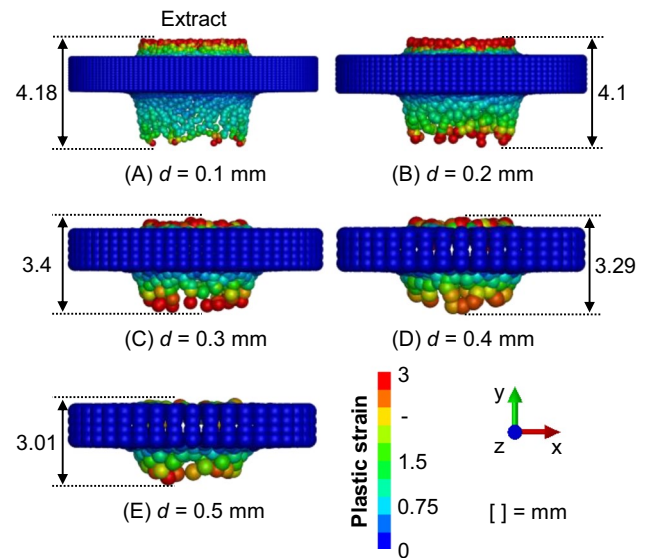
Fig. 3 Plastic strain distribution of the SPG friction drilling simulation at the extract for different particle distances

more accurately and therefore more material is available to form the bushing length.

Figure 4 displays the axial force (A), the torque (B) and the temperature at the specimen surface (C) for different particle distances. Increasing the particle distance from 0.1 mm to 0.5 mm leads to a decrease in the axial force, whereas the torque is almost unaffected by the particle distance. Similar to the axial force, the temperature at the specimen surface drops for higher particle distances. Due to a smaller particle distance, the forming can be mapped more precisely and therefore the axial force as well as the temperature are closer to the experimental results.

The influence of the particle distance on the maximum axial force, maximum temperature and final bushing length compared to the experimental values is depicted in Fig. 5. To evaluate the deviation, the calculation time is also plotted in the figure. A clear reduction tendency of the deviation for all shown parameters is visible as the particle distance decreases from 0.5 to 0.1 mm. However, the calculation time increases rapidly with reduced particle distance. Especially from a particle distance of 0.2 to 0.1 mm, the calculation time rises from 22 to 267 h using 16 CPU for all models. Due to the long calculation time for a particle distance of 0.1 mm, the particle distance of 0.2 mm provides a resource-efficient solution with a good agreement compared to the experiment, since all deviations are smaller than 5%.
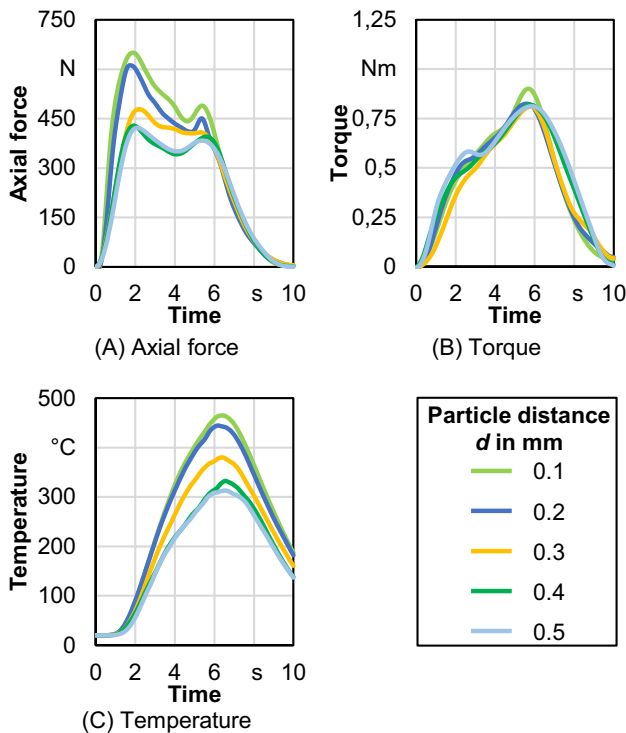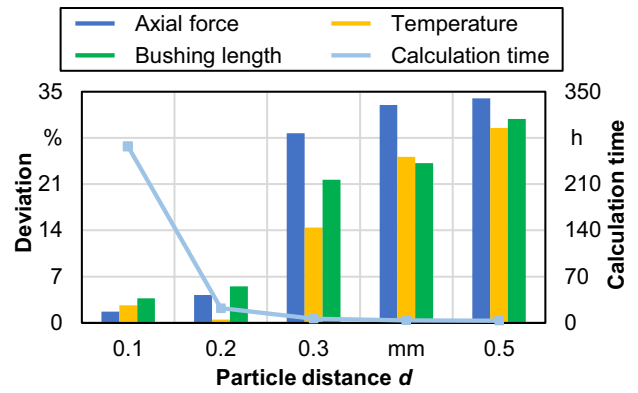
Fig. 5 Influence of the particle distance on the deviation of calculated maximum axial force, temperature and bushing length from the experimental values

Variation of the friction coefficient

A variation of the friction coefficient for multiple values between 0.1 and 0.5 was performed, whereas the other parameters were the same. Figure 6 shows a contour plot of the maximum process temperature. The maximum temperature occurs when the cylindrical part of the friction drill enters the specimen at the breakthrough and is therefore plotted. As expected, the higher the friction coefficient, the higher the maximum temperature during friction drilling. Figure 6 also displays the plastic strain distribution at the extract for the variation of the friction coefficient. The plastic strain shows a positive correlation to the temperature
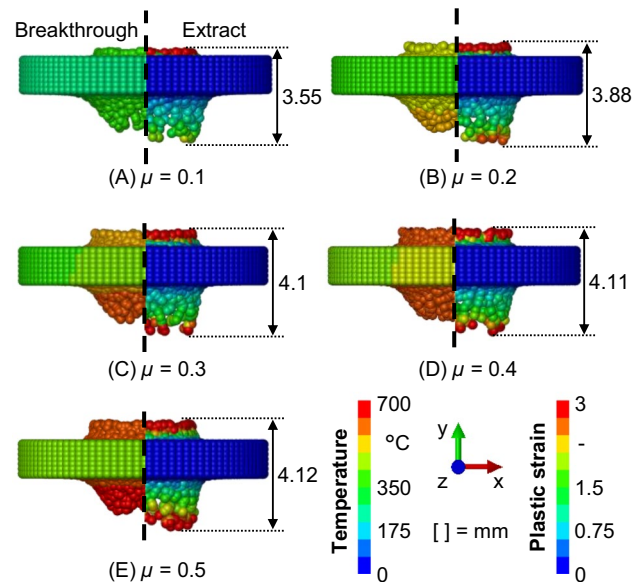
Fig. 4 Comparison of different process quantities for the SPG friction drilling simulation under varying particle distance

Fig. 6 Maximum process temperature distribution after the breakthrough (left) and plastic strain distribution after the extract (right) of the SPG friction drilling simulation for different friction coefficients

development. With higher friction coefficients, the magnitude of the plastic strain as well as the amount of highly formed particles rises in the upper and lower bushing. Similarly, the length of the bushing rises with an increasing friction coefficient from 3.55 to 4.12 mm for the friction coefficients of 0.1 up to 0.5. Whereas the highest increase in length is up to a friction coefficient of 0.3, the bushing length only increases slowly for higher friction coefficients. The higher temperature results in both, a longer upper and lower bushing, because of the better formability of the material at elevated temperatures.

A comparison of the axial force (A), the torque (B) and the temperature at the specimen surface (C) is outlined in Fig. 7 for the variation of the friction coefficient. As shown before, the maximum temperature increases with the friction coefficient and thus the axial force decreases, since commonly warmer material needs less force to be formed. In contrast, the torque increases for higher friction coefficients due to higher resistance caused by more friction.

Figure 8 summarises the deviation of the maximum axial force, maximum temperature and final bushing length from the SPG simulations with different friction coefficients to the experimental values. For the axial force and the temperature, the same trend of the deviation is noticeable: increasing the friction coefficient from 0.1 the deviations reduce with the minimum at a friction coefficient of 0.3. For a further increase of the friction coefficient to 0.5 the deviations rise
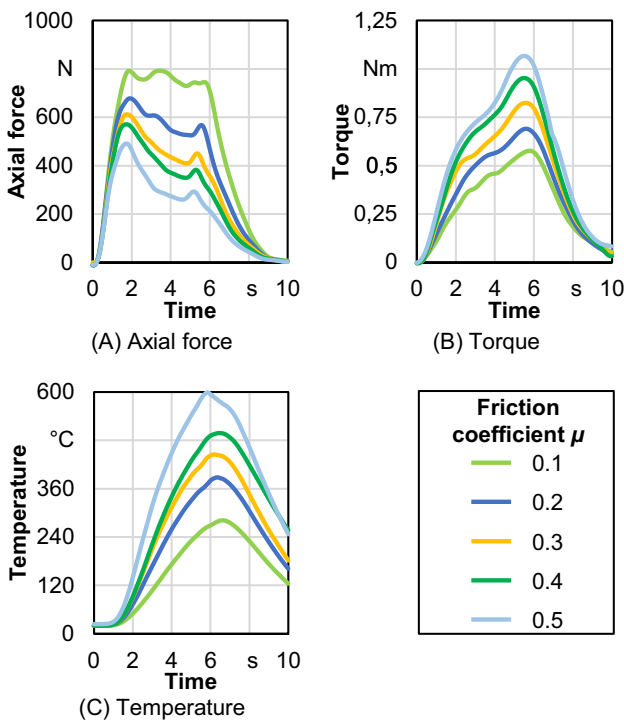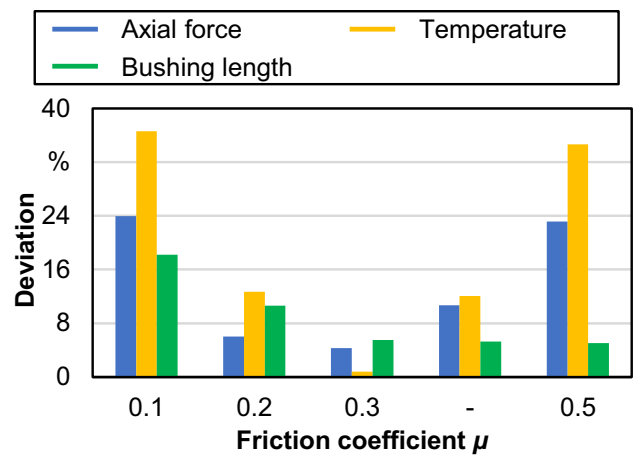

Fig. 8 Influence of the friction coefficient on the deviation of calculated maximum axial force, temperature and bushing length from the experimental values

again. The deviation of the bushing length on the contrary exhibits decreasing values for coefficients up to 0.3 and remains almost constant for higher friction coefficients. Therefore, the friction coefficient 0.3 provides the results with the best agreement compared to the experiment with all deviations being less than 6%.

Comparison to the friction drilling experiment

A comparison of the experimental data for friction drilling HX220 and the numerical results from the SPG simulation was performed using a particle distance of 0.2 mm and a friction coefficient of 0.3 due to the best fit. The sheet thickness, the feed rate and the rotational speed were set to 1.2 mm, 50 mm/min and 5800 rpm comparable to the experiment. Optical images from the experiments are contrasted to the corresponding SPG simulation in Fig. 9 for different forming depths such as entrance of the friction drill into the specimen (A), breakthrough (B) and extraction (C).

The presented variable of the SPG simulation is the temperature distribution during forming. The resulting bushing in the experiment is about 4.34 mm, while the bushing in the SPG simulation measures 4.1 mm and is about 5% shorter. In the FE simulation performed in a previous work, a bushing length of only 3.35 mm was created due to element deletion [55]. Hence, the bushing length is more realistic using the SPG simulation compared to an FE simulation of friction drilling. Due to the used bond failure mechanism, no elements and therefore no information is deleted while simulating the material separation during friction drilling. Considering the temperature development in the specimen, the maximum temperature occurs at the time when the cylindrical part of the friction drill is in contact with the specimen and the breakthrough is performed. The reason for this
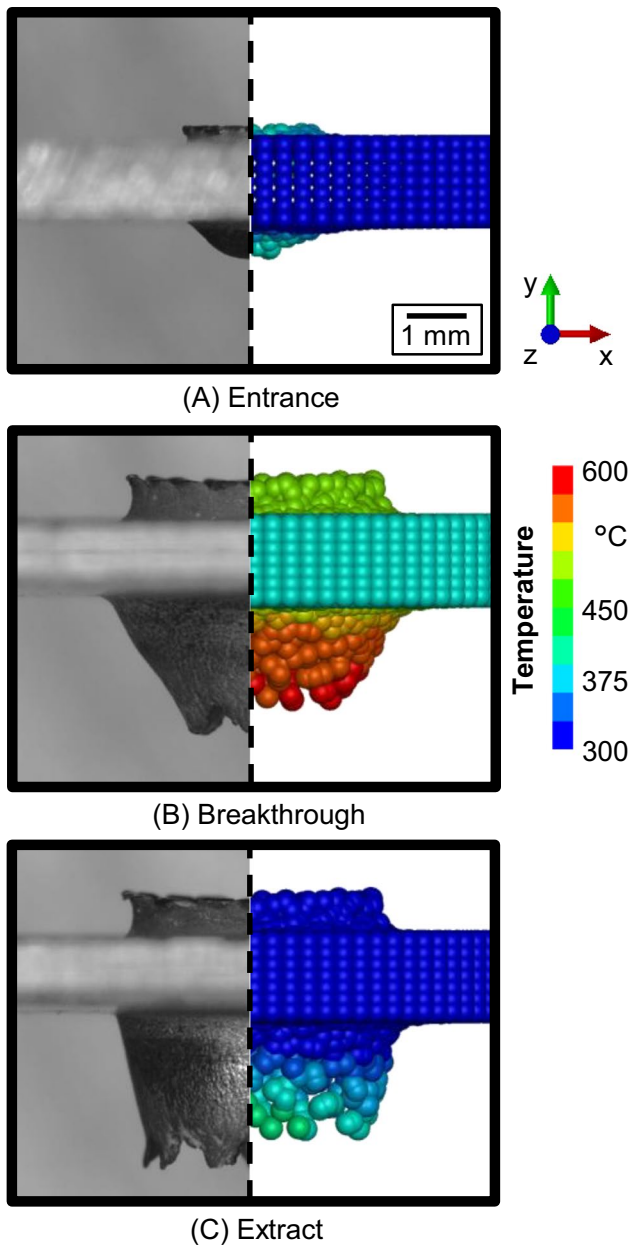

Fig. 7 Comparison of different process quantities for the SPG friction drilling simulation under varying friction coefficient

(A) Entrance

(B) Breakthrough

(C) Extract

Fig. 9 Optical images and temperature distribution of the SPG friction drilling simulation at different forming depths
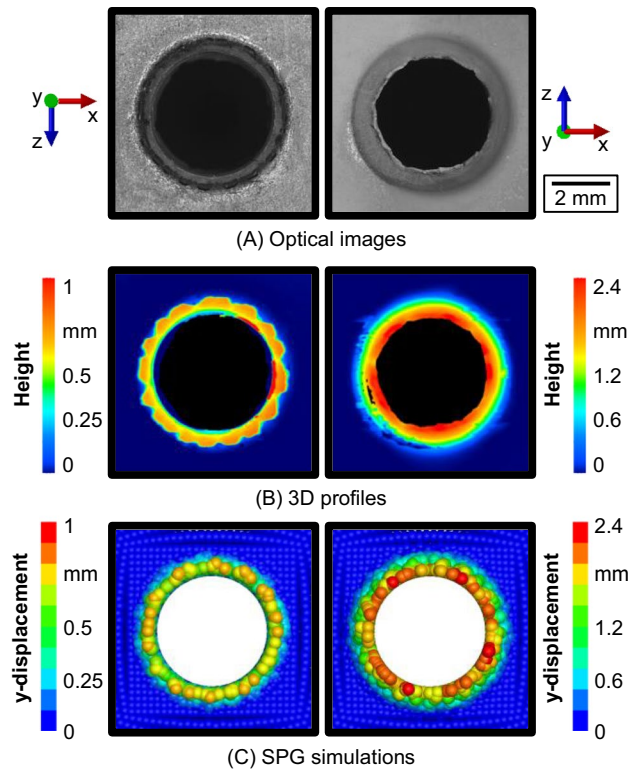

(A) Optical images

(B) 3D profiles

(C) SPG simulations

Fig. 10 Qualitative comparison of the upper (left) and lower bushing (right) of the experiments and SPG friction drilling simulation

is most likely that at this time the biggest area of the tool is in contact with the specimen. For a further overview and to provide a qualitative comparison, optical images as well as 3D profiles obtained by the performed experiments and the y-displacement distribution from the SPG simulation are shown in Fig. 10 for the upper as well as the lower bushing.

Figure 11 displays the axial force (A) as well as the temperature at the specimen surface about 4 mm from the centre (B) for the experiments and the SPG simulation. For both experimental process quantities, three curves are plotted in order to guarantee statistical verification. All in all, a very

good agreement between the experimental and the numerical axial force was achieved. After a rapid growth of the axial force, the maximum is reached, which decreases as the process continues, and after about 5 s a second peak occurs. The maximum experimental force is about 639 N and the maximum in the SPG simulation is 612 N, resulting in an error of about 4.2%. As for the axial force, the temperature development as well as the maximum temperature of about 445 °C from the experiment could be mapped using the SPG
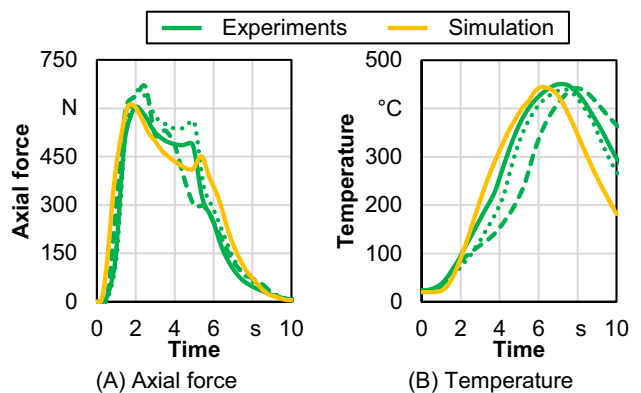

(A) Axial force

(B) Temperature

Fig. 11 Comparison of different experimental and numerical process quantities

simulation with a good agreement. The maximum temperature in the SPG simulation is 444 °C which results in an error of about 0.3%.

To show that the applied mass scaling does not affect the results, the percentage of the kinetic energy on the internal energy is plotted in Fig. 12 for the SPG friction drilling simulation. It is shown, that the kinetic energy does not exceed a fraction of 5% of the internal energy, which is recommended as a threshold value in the literature [57]. In the early stages of the analysis a maximum of 3.56% is reached, which decreases rapidly up to values in the order of the magnitude of 0.02% during the further friction drilling simulation. Therefore, it is concluded that the used mass scaling has no significant effect on the simulation results. When using time scaling, the time is reduced to efficiently calculate a numerical problem and the material strain rates calculated in the simulation are artificially high by the same factor applied to decrease the time. Since the material was modelled strain rate independent according to [55], there is no conflict to it regarding the time scaling. Based on these results, a study of the input parameters was performed varying sheet thickness, feed rate and rotational speed to show their influence on the resulting parameters of the SPG simulation.

Investigation of the friction drilling input parameters

Influence of the sheet thickness

Figure 13 displays the variation of the sheet thickness between 1, 1.2 and 1.4 mm. All other parameters were set as before. On the left, the maximum temperature of the process at the breakthrough and on the right the plastic strain distribution at the extract is shown for the different sheet thicknesses. Comparing the maximum temperature for each sheet thickness, only a small increase in the temperature for higher sheet thicknesses can be observed. The upper and lower bushing lengths increase as to be expected for thicker
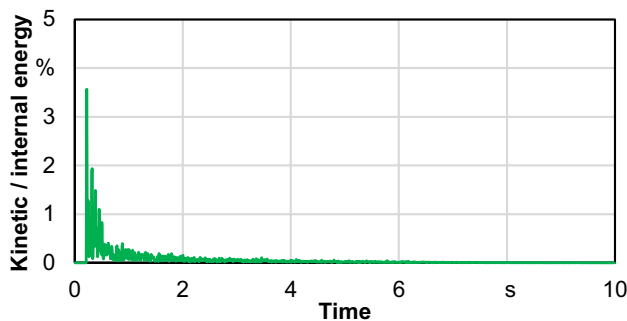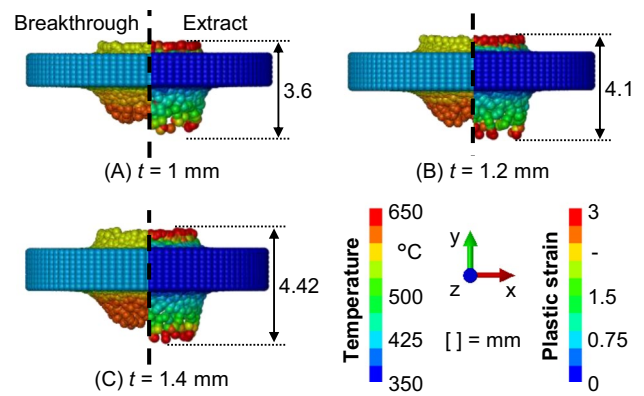

Fig. 13 Maximum process temperature distribution after the breakthrough (left) and plastic strain distribution after the extract (right) of the SPG friction drilling simulation for different sheet thicknesses

specimens, since more material can be displaced. The total bushing lengths are 3.60, 4.1 and 4.42 mm.

The variation of the sheet thickness and its influence on the axial force (A), torque (B) and temperature at the specimen surface (C) are plotted in Fig. 14. Increasing the sheet thickness from 1 to 1.4 mm leads to a significant rise in the axial force as well as the torque, since more material is present that can be formed. The temperature increases along with the sheet thickness, but only marginally, as shown
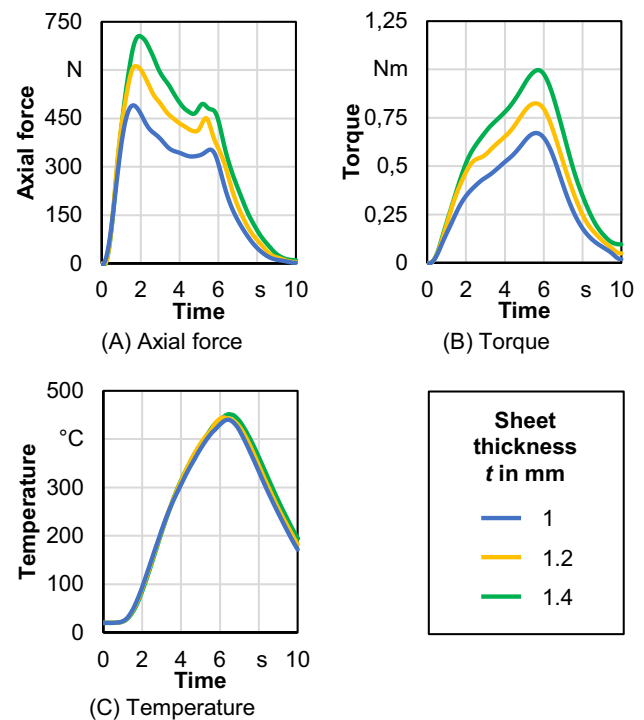

Fig. 12 Fraction of kinetic energy on the internal energy for the SPG friction drilling simulation

Fig. 14 Comparison of different process quantities for the SPG friction drilling simulation under varying sheet thickness

before in Fig. 13. These influences of sheet thickness on the process were also detected experimentally by Gies [58].

Influence of the feed rate

The Influence of the feed rate was studied, which was set to 30, 50 and 70 mm/s while all other parameters were kept constant. The calculated maximum temperature at the breakthrough and the plastic strain at the extract are shown in Fig. 15 as contour plots. As plotted on the left side, the temperature reaches lower values for an increase in feed rate. Due to a lower feed rate, the friction drill is longer in contact with the specimen, generating a higher temperature due to friction. The right side of the figure depicts that the length of the bushing decreases for higher feed rates as the plastic strain is lower. The resulting lengths are 4.14, 4.10 and 4.01 mm.

The process quantities axial force (A), torque (B) and temperature at the specimen surface (C) are displayed in Fig. 16 for the feed rates 30, 50 and 70 mm/min keeping the rotational speed constant. Since the contact time between friction drill and specimen is reduced for higher feed rates, the temperature decreases with increasing feed rate. In accordance with the temperature decrease, the axial force and the torque increase for elevated feed rates, which was also experimentally shown by Gies [58].

Influence of the rotational speed

The process sensitivity regarding the rotational speed was also investigated. Studied speeds were 4800, 5800 and 6800 rpm. As before, the maximum process temperature distribution at the breakthrough as well as the plastic strain distribution at the extract are evaluated and shown in Fig. 17. Contrary to the variation of the feed rate, the temperature
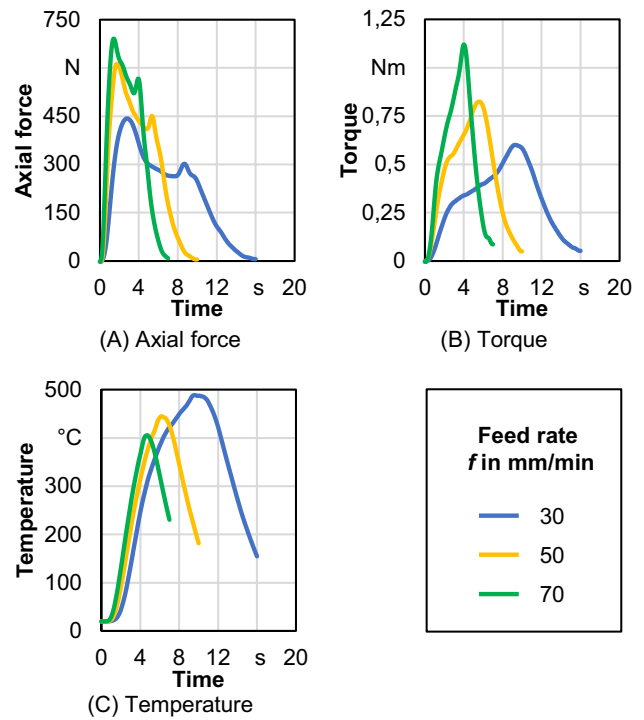

Fig. 16 Comparison of different process quantities for the SPG friction drilling simulation under varying feed rate

rises when the rotational speed is increased, since more rotations are performed at the same time for higher speeds. The higher temperature leads to increasing bushing lengths of 3.35, 4.1 and 4.23 mm, which corresponds to the experimental tendency investigated by Gies [58].

The variation of the rotational speed with constant feed rate is shown in Fig. 18. In (A) the axial force, in (B) the torque and in (C) the temperature at the specimen surface are displayed. Contrary to the variation of the feed rate, the axial force and the torque decrease for higher rotational speeds,
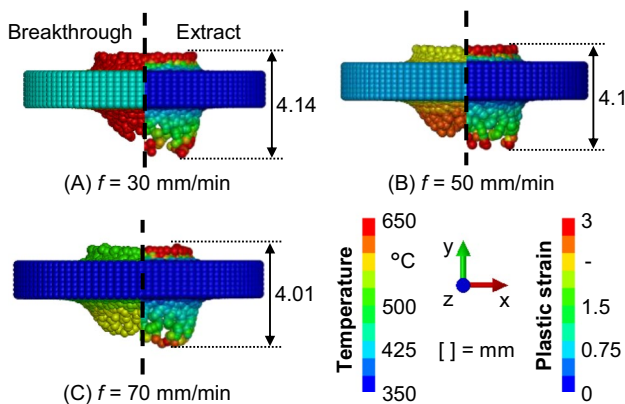

Fig. 15 Maximum process temperature distribution after the breakthrough (left) and plastic strain distribution after the extract (right) of the SPG friction drilling simulation for different feed rates
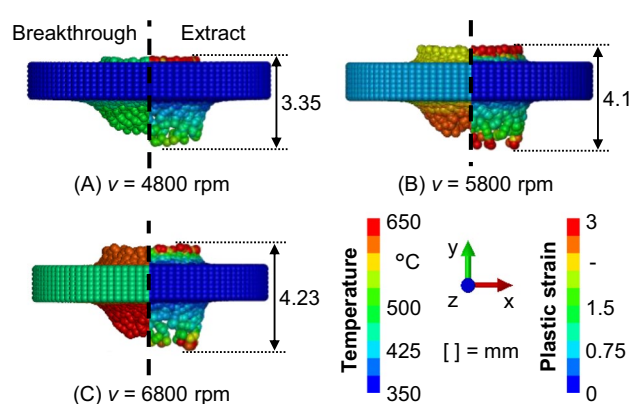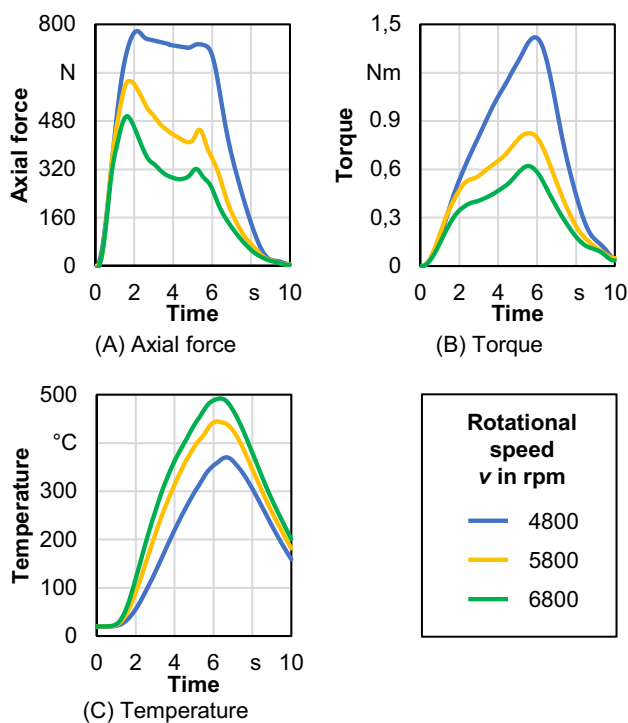

Fig. 17 Maximum process temperature distribution after the breakthrough (left) and plastic strain distribution after the extract (right) of the SPG friction drilling simulation for different rotational speeds

Fig. 18 Comparison of different process quantities for the SPG friction drilling simulation under varying rotational speed

since the temperature rises due to the more frequent contact between friction drill and specimen.

Summary

In this research, the SPG method was applied successfully for modelling a friction drilling process. The SPG model was verified by comparison to experimental results regarding axial force, surface temperature and bushing length with errors less than 5%. Due to the meshless particle property and displacement smoothing scheme of the SPG method, the extremely large deformations during friction drilling were mapped without problems such as mesh distortion in traditional FEM. A further advantage is that the bond-based failure mechanism enabled the simulation of a forming process including material failure without loss of material in terms of information by element deletion.

In a first applicability study the particle distance 0.2 mm and a friction coefficient of 0.3 were found to represent the experiments best regarding the axial force, process temperature and bushing length of the specimen. A further performed sensitivity study of input parameters also showed interesting outcomes. The numerical results demonstrate the effect of sheet thickness, feed rate and rotational speed on the process in a reasonable way. A thicker sheet led to a higher bushing length, axial force and torque, but similar process temperatures for all sheet thicknesses. The feed rate and rotational speed showed opposite effects. The higher the feed rate, the lower the temperature as well as the bushing length and the higher the axial force as well as the torque. With a high rotational speed, temperature and bushing length are rising, whereas forming force and torque are falling. All in all, the usage of the SPG method for friction drilling was validated by experimental data and showed great potential for numerical representation of friction drilling. However, in the future further work should be performed regarding the use of SPG method in forming simulation of processes with extreme deformations.

Declarations

References

1. Heiler R (2019) Flow drilling technology and thread forming - an economical and secure connection in hollow sections and thin-walled components. E3S Web Conf 97:06033. https://doi.org/10.1051/e3sconf/20199706033
2. Hynes N, Kumar R (2017) Process optimization for maximizing bushing length in thermal drilling using integrated ANN-SA approach. J Braz Soc Mech Sci Eng 39(12):5097–5108
3. Rajesh N, Hynes J, Kumar R, Sujana JAJ (2017) Optimum bushing length in thermal drilling of galvanized steel using artificial neural network coupled with genetic algorithm. Mater Tehnol 51(5):813–822. https://doi.org/10.17222/mit.2016.290
4. Narayana Moorthy N, Kanish TC (2020) Fuzzy logic-based model for predicting surface roughness of friction drilled holes. In: Soft computing for problem solving. Springer, pp 251–260

5. Behrens B-A, Uhe J, Wester H, Stockburger E (2020) Hot forming limit curves for numerical press hardening simulation of AISI 420C, pp 350–355. https://doi.org/10.37904/metal.2020.3667

6. Behrens B-A, Rosenbusch D, Wester H, Stockburger E (2022) Material characterization and modeling for finite element simulation of press hardening with AISI 420C. J Mater Eng Perform 31(1):825–832. https://doi.org/10.1007/s11665-021-06216-y

7. Miller SF, Shih AJ (2007) Thermo-mechanical finite element modeling of the friction drilling process. J Manuf Sci Eng 129(3):531–538. https://doi.org/10.1115/1.2716719

8. Krasauskas P, Kilikevičius S, Česnavičius R, Pačenga D (2015) Experimental analysis and numerical simulation of the stainless AISI 304 steel friction drilling process. Mechanics 20(6):590–595. https://doi.org/10.5755/j01.mech.20.6.8664

9. Pan X, Wu CT, Hu W, Wu Y (2019) A momentum-consistent stabilization algorithm for Lagrangian particle methods in the thermo-mechanical friction drilling analysis. Comput Mech 64(3):625–644

10. Chen J-S, Pan C, Wu C-T, Liu WK (1996) Reproducing kernel particle methods for large deformation analysis of non-linear structures. Comput Methods Appl Mech Eng 139(1–4):195–227

11. Hillman M, Chen J-S, Chi S-W (2014) Stabilized and variationally consistent nodal integration for meshfree modeling of impact problems. Comput Part Mech 1(3):245–256

12. Rabczuk T, Belytschko T (2004) Cracking particles: a simplified meshfree method for arbitrary evolving cracks. Int J Numer Meth Eng 61(13):2316–2343

13. Gingold RA, Monaghan JJ (1977) Smoothed particle hydrodynamics: theory and application to non-spherical stars. Mon Not R Astron Soc 181(3):375–389

14. Lucy LB (1977) A numerical approach to the testing of the fission hypothesis. Astron J 82:1013–1024

15. Violeau D (2012) Fluid mechanics and the SPH method: theory and applications. Oxford University Press

16. Ba K, Gakwaya A (2018) Thermomechanical total Lagrangian SPH formulation for solid mechanics in large deformation problems. Comput Methods Appl Mech Eng 342:458–473. https://doi.org/10.1016/j.cma.2018.07.038

17. Belytschko T, Guo Y, Kam Liu W, Ping Xiao S (2000) A unified stability analysis of meshless particle methods. Int J Numer Methods Eng 48(9):1359–1400

18. Belytschko T, Lu YY, Gu L (1994) Element-free Galerkin methods. Int J Numer Meth Eng 37(2):229–256

19. Liu WK, Jun S, Zhang YF (1995) Reproducing kernel particle methods. Int J Numer Meth Fluids 20(8–9):1081–1106

20. Chen J-S, Wu C-T, Yoon S, You Y (2001) A stabilized conforming nodal integration for Galerkin mesh-free methods. Int J Numer Meth Eng 50(2):435–466

21. Wu CT, Koishi M, Hu W (2015) A displacement smoothing induced strain gradient stabilization for the meshfree Galerkin nodal integration method. Comput Mech 56(1):19–37

22. Wu C-T, Chi S-W, Koishi M, Wu Y (2016) Strain gradient stabilization with dual stress points for the meshfree nodal integration method in inelastic analyses. Int J Numer Meth Eng 107(1):3–30

23. Wu CT, Wu Y, Crawford JE, Magallanes JM (2017) Three-dimensional concrete impact and penetration simulations using the smoothed particle Galerkin method. Int J Impact Eng 106:1–17

24. Prakash M, Cleary P (2006) Modelling of cold metal extrusion using SPH, presented at the Fifth international conference on CFD in the process industries. Accessed: Jun. 01, 2022. [Online]. Available: https://publications.csiro.au/rpr/pub?list=BRO&pid=procite:fb627e86-ea66-4fce-96a4-9b3e8bfab5fa

25. Reddy BD (Ed) (2008) The potential for SPH modelling of solid deformation and fracture, vol 11. Springer Netherlands, Dordrecht. https://doi.org/10.1007/978-1-4020-9090-5

26. Bonet J, Kulasegaram S (2000) Correction and stabilization of smooth particle hydrodynamics methods with applications in metal forming simulations. Int J Numer Meth Engng 47(6):1189–1214. https://doi.org/10.1002/(SICI)1097-0207(20000228)47:6%3c1189::AID-NME830%3e3.0.CO;2-I

27. Chen J-S, Pan C, Roque CMOL, Wang H-P (1998) A Lagrangian reproducing kernel particle method for metal forming analysis. Comput Mech 22(3):289–307. https://doi.org/10.1007/s004660050361

28. Xiong S, Li CS, Rodrigues JMC, Martins PAF (2005) Steady and non-steady state analysis of bulk forming processes by the reproducing kernel particle method. Finite Elem Anal Des 41(6):599–614. https://doi.org/10.1016/j.finel.2004.10.003

29. Li G, Sidibe K, Liu G (2004) Meshfree method for 3D bulk forming analysis with lower order integration scheme. Eng Anal Boundary Elem 28(10):1283–1292. https://doi.org/10.1016/j.enganabound.2003.11.005

30. Cui Q, Liu X, Wang G (2007) Splitting rolling simulated by reproducing kernel particle method. J Iron Steel Res Int 14(3):42–46. https://doi.org/10.1016/S1006-706X(07)60041-7

31. Wang H, Li G, Han X, Zhong ZH (2007) Development of parallel 3D RKPM meshless bulk forming simulation system. Adv Eng Softw 38(2):87–101. https://doi.org/10.1016/j.advengsoft.2006.08.002

32. Liu HS, Xing ZW, Yang YY (2010) Simulation of sheet metal forming process using reproducing kernel particle method. Int J Numer Meth Biomed Engng 26(11):1462–1476. https://doi.org/10.1002/cnm.1229

33. Li G, Belytschko T (2001) Element-free Galerkin method for contact problems in metal forming analysis. Eng Comput 18(1/2):62–78. https://doi.org/10.1108/02644400110365806

34. Xiong S, Rodrigues JMC, Martins PAF (2004) Application of the element free Galerkin method to the simulation of plane strain rolling. Eur J Mech A Solids 23(1):77–93. https://doi.org/10.1016/j.euromechsol.2003.10.002

35. Shangwu X, Rodrigues JMC, Martins PAF (2005) Simulation of plane strain rolling through a combined element free Galerkin–boundary element approach. J Mater Process Technol 159(2):214–223. https://doi.org/10.1016/j.jmatprotec.2004.05.008

36. Guan Y, Zhao G, Wu X, Lu P (2007) Massive metal forming process simulation based on rigid/visco-plastic element-free Galerkin method. J Mater Process Technol 187–188:412–416. https://doi.org/10.1016/j.jmatprotec.2006.11.075

37. Liu Y, Chen J, Yu S, Li C (2008) Numerical simulation of three-dimensional bulk forming processes by the element-free Galerkin method. Int J Adv Manuf Technol 36(5–6):442–450. https://doi.org/10.1007/s00170-006-0865-z

38. Lu P, Zhao G, Guan Y, Wu X (2008) Bulk metal forming process simulation based on rigid-plastic/viscoplastic element free Galerkin method. Mater Sci Eng, A 479(1–2):197–212. https://doi.org/10.1016/j.msea.2007.06.059

39. Liu L, Dong X, Li C (2009) Adaptive finite element-element-free Galerkin coupling method for bulk metal forming processes. J Zhejiang Univ Sci A 10(3):353–360. https://doi.org/10.1631/jzus.A0820286

40. Yuan B, Fang W, Li J, Cai Y, Qu Z, Wang Z (2016) A coupled finite element-element-free Galerkin method for simulating viscous pressure forming. Eng Anal Boundary Elem 68:86–102. https://doi.org/10.1016/j.enganabound.2016.04.003

41. Wang Z, Yuan B (2014) Numerical analysis of coupled finite element with element-free Galerkin in sheet flexible-die forming.

Trans Nonferrous Met Soc China 24(2):462–469. https://doi.org/10.1016/S1003-6326(14)63083-1

42. Alfaro I, Bel D, Cueto E, Doblaré M, Chinesta F (2006) Three-dimensional simulation of aluminium extrusion by the α-shape based natural element method. Comput Methods Appl Mech Eng 195(33–36):4269–4286. https://doi.org/10.1016/j.cma.2005.08.006

43. Filice L, Alfaro I, Gagliardi F, Cueto E, Micari F, Chinesta F (2009) A preliminary comparison between finite element and meshless simulations of extrusion. J Mater Process Technol 209(6):3039–3049. https://doi.org/10.1016/j.jmatprotec.2008.07.013

44. Lu P, Shu Y, Lu D, Jiang K, Liu B, Huang C (2017) Research on natural element method and the application to simulate metal forming processes. Procedia Eng 207:1087–1092. https://doi.org/10.1016/j.proeng.2017.10.1135

45. Yoon S, Chen J-S (2002) Accelerated meshfree method for metal forming simulation. Finite Elem Anal Des 38(10):937–948. https://doi.org/10.1016/S0168-874X(02)00086-0

46. Kwon K-C, Park S-H, Youn S-K (2005) The least-squares mesh-free method for elasto-plasticity and its application to metal forming analysis. Int J Numer Meth Eng 64(6):751–788. https://doi.org/10.1002/nme.1384

47. Hah Z-H, Youn S-K (2015) Eulerian analysis of bulk metal forming processes based on spline-based meshfree method. Finite Elem Anal Des 106:1–15. https://doi.org/10.1016/j.finel.2015.07.004

48. Wu CT, Bui TQ, Wu Y, Luo T-L, Wang M, Liao C-C, Chen P-Y, Lai Y-S (2018) Numerical and experimental validation of a particle Galerkin method for metal grinding simulation. Comput Mech 61(3):365–383

49. Huang L, Wu Y, Huff G, Huang S, Ilinich A, Freis AK, Luckey G (2018) Simulation of self-piercing rivet insertion using smoothed particle Galerkin method

50. Wu Y, Wu CT (2018) Simulation of impact penetration and perforation of metal targets using the smoothed particle Galerkin method. J Eng Mech 144(8):04018057

51. Wu Y, Wu CT, Hu W (2017) Modeling of ductile failure in destructive manufacturing processes using the smoothed particle galerkin method. In: Proceedings of the China LS-DYNA Users Conference, Shanghai, China, pp 23–25

52. Pan X, Wu CT, Hu W, Wu Y (2019) A momentum-consistent stabilization algorithm for Lagrangian particle methods in the thermo-mechanical friction drilling analysis. Comput Mech 64(3):625–644. https://doi.org/10.1007/s00466-019-01673-8

53. Wu CT, Wu Y, Lyu D, Pan X, Hu W (2020) The momentum-consistent smoothed particle Galerkin (MC-SPG) method for simulating the extreme thread forming in the flow drill screw-driving process. Comp Part Mech 7(2):177–191. https://doi.org/10.1007/s40571-019-00235-2

54. Johnson GR, Cook WH (1985) Fracture characteristics of three metals subjected to various strains, strain rates, temperatures and pressures. Eng Fract Mech 21(1):31–48

55. Behrens B-A, Dröder K, Hürkamp A, Droß M, Wester H, Stockburger E (2021) Finite element and finite volume modelling of friction drilling HSLA steel under experimental comparison. Materials 14(20):5997. https://doi.org/10.3390/ma14205997

56. Eliseev A, Kolubaev E (2021) Friction drilling: a review. Int J Adv Manuf Technol 116(5–6):1391–1409. https://doi.org/10.1007/s00170-021-07544-y

57. Abaqus Documentation (2017) Version 2017, Dassault Systémes Simulia Corp., Providence, RI

58. Gies C (2006) Evaluation der Prozesseinflussgrößen beim Fließlochformen mittels DoE. kassel university press GmbH

Publisher's note Springer Nature remains neutral with regard to jurisdictional claims in published maps and institutional affiliations.